Solar Energy Materials & Solar Cells 299 (2026) 114169

Contents lists available at ScienceDirect

Solar Energy Materials and Solar Cells

journal homepage: www.elsevier.com/locate/solmat

Combining physical- and scenario-based modeling to identify tolerable degradation rates of perovskite in monolithic two-terminal perovskite/silicon tandem modules

Youri Blom *, Rudi Santbergen, Olindo Isabella, Malte Ruben Vogt *

Delft University of Technology, Mekelweg 4, Delft, 2628CD, The Netherlands

ARTICLE INFO

Keywords:
Degradation modeling
Perovskite/silicon modules
Lifetime energy yield
Environmental impact
Reliability

ABSTRACT

As crystalline silicon (c-Si) solar cells approach their theoretical efficiency limit, the perovskite/silicon (PerSi) tandem technology offers a promising solution for further improving the efficiency of photovoltaic (PV) modules. However, as perovskite cells are facing stability issues, it is unclear whether PerSi modules will have a larger lifetime energy yield (LEY) than c-Si modules. In this work, we present a novel methodology to simulate the LEY of PerSi tandem devices, accounting for environmental stress factor-dependent degradation across four different climates. Our approach combines a physics-based analytical degradation model for components shared with c-Si modules and a scenario-based degradation model for the perovskite top cell. This method enables us to identify the tolerable degradation rate (k_{tol}) of the perovskite cell under different scenarios and climatic conditions. We find that k_{tol} is lowest when degradation occurs in the short-circuit current, reaching a minimum value of 1.2% per year in Delft (the Netherlands). Additionally, we demonstrate that k_{tol} inversely depends on the module lifetime, reaching values up 7.6% per year in Lagos (Nigeria). Moreover, we show that module efficiency (η_{mod}) significantly impacts k_{tol}. For instance, increasing η_{mod} from 28.0% to 32.9% raises k_{tol} by approximately 50%. Additionally, we propose a simplified model that can predict k_{tol} without the computationally intensive simulations, which has a root-mean-square error of 0.34% per year. Lastly, environmental impact assessments reveal that PerSi modules are more sustainable in all impact categories when the degradation rate is 80% of k_{tol} for LEY.

1. Introduction

To surpass the theoretical efficiency limit of 29.5% [1,2] for conventional crystalline silicon (c-Si) solar cells, the perovskite/silicon (PerSi) tandem technology offers a promising solution. This technology has practical and theoretical efficiency limits of 39.5% [3] and 42% [4,5], respectively, with a record efficiency of 34.6% [6] already demonstrated.

However, perovskite-based solar cells face stability issues [7,8], which would affect the lifetime of PerSi modules. Since both efficiency and lifetime are crucial for total electricity generation [9], both factors must be considered when comparing c-Si and PerSi systems.

A key determinant of a photovoltaic (PV) system's lifetime is its degradation rate (k), which quantifies the irreversible power loss compared to its initial power [10]. k can be predicted using data-driven or physics-based models [11], both of which require calibration with outdoor data. Unfortunately, current reported outdoor experiments involving PerSi technology are mostly limited to small-scale cells operating for a maximum of one year [12–15], making conventional approaches unsuitable.

An alternative approach involves modeling energy yield under different degradation scenarios to identify tolerable degradation rates. Qian et al. [16] introduced a method that separates the degradation rates of perovskite (k_{per}) and silicon (k_{sil}). In Qian's approach both k_{per} and k_{sil} are assumed scenario based losses in output power without specifying the underlying degradation mechanisms. They found that k_{per} values between 0.5% and 0.9% per year are acceptable for two-terminal PerSi cells to outperform c-Si cells. Moreover, they observed that a 2% absolute increase in tandem efficiency extends the tolerable k_{per} by 1%.

Similarly, Orooj and Paetzold [17] adjusted parameters in the equivalent circuit of a PerSi tandem cell to study their effects on standard test conditions (STC) and energy yield (EY). They found that degradation in the short-circuit current density of the perovskite subcell had the

* Corresponding authors.
E-mail addresses: Y.Blom@tudelft.nl (Y. Blom), M.R.Vogt@tudelft.nl (M.R. Vogt).

https://doi.org/10.1016/j.solmat.2026.114169
Received 7 July 2025; Received in revised form 11 November 2025; Accepted 7 January 2026
Available online 28 January 2026

greatest impact on tandem performance. Additionally, they identified the tolerable degradation rates for the different degradation scenarios.

Lastly, Aydin et al. [18] conducted a simplified Levelized Cost of Electricity analysis to determine acceptable degradation rates for PerSi tandems. They concluded that if the tandem degradation rate is 2% per year and there are no additional costs compared to c-Si modules, the module efficiency must exceed 32% to remain competitive.

While these studies offer valuable insights into tolerable k_{per} values, none accounts for climate dependency in degradation rates. Given that k_{sil} varies across different climates [19], it is likely that k_{per} tolerances also vary by location. Moreover, in two-terminal PerSi tandem cells, where the voltages of both subcells are combined, a single degradation rate is insufficient to describe performance loss, as shown in Appendix A.

In this work, we propose a new approach to determine tolerable k_{per} values. We develop an analytical model for the silicon bottom cell, fitting and validating it with experimental data. A scenario-based approach is then used to model degradation in the perovskite cell. By simulating EY for various k_{per} values, we identify tolerable rates across different locations. Additionally, a simplified model is developed that can predict the tolerable degradation rates without performing the computationally intensive simulations. Finally, we examine how tolerable k_{per} values change with higher cell efficiencies and assess the environmental impact of PerSi and c-Si modules.

It is important to note that this study only covers the analysis for monotlithic two-terminal (2T) PerSi modules, as these devices are most similar to the single junction reference modules. Future work can be done to explore how the tolerable degradation rate changes for different terminal configurations.

2. Methodology

To identify tolerable values for k_{per}, we extend the PVMD Toolbox [20] by developing a methodology to simulate degradation. The PVMD Toolbox is a modeling framework designed to predict the EY of various PV systems by simulating key aspects of their performance. The simulation process begins by calculating the optical response of each subcell for the relevant wavelength range (300–1200 nm), which helps determine the incoming irradiance. This irradiance data is then used to calculate the temperature of each cell throughout the year. Finally, the electrical performance is simulated to obtain the EY of the PV module and the system afterwards. Full details and validation of the PVMD Toolbox have been documented in previous studies [20–23].

To predict the lifetime energy yield (LEY) of a PV system, we extend the annual PVMD simulation by adjusting input parameters to account for degradation. Fig. 1a illustrates the degradation modeling methodology.

We use an analytical model to simulate degradation in the silicon bottom cell, encapsulation, and contact resistance. Since these components are similar to those in single-junction c-Si modules, available outdoor data can be used to calibrate the model effectively.

For the perovskite top cell, a different approach is required. Due to the lack of large-scale outdoor data for perovskite modules, we adopt a scenario-based approach. The simulation of the top cell is adjusted based on three different scenarios to explore tolerable degradation rates.

The performance of the top and bottom cell is modeled using a one-diode equivalent circuit model with two resistors [24–27]. The behavior of this model can be described with 5 parameters, namely the photo-generated current (I_{ph}), the diode saturation current (I_0), the diode ideality factor (n), the shunt resistance (R_{shunt}), and the series resistance (R_s). To simulate a tandem cell, both circuits are connected in series with an additional resistor to represent the interconnection (R_{con}).

2.1. Analytical modeling

In literature, various analytical models have been developed to predict performance loss in c-Si modules [28,29]. However, these models typically produce only a single value for k without distinguishing between losses in voltage or current. For this reason, they are unsuitable for tandem devices.

To address this limitation, we develop a new analytical model that not only provides k but also simulates losses in the absorption profile and the current–voltage (IV) curve. This model accounts for different degradation types and stress factors, simulating their impact on module performance through analytical equations. The degradation mechanisms included in this model are discoloration, moisture-induced degradation (MID), thermal cycling-induced degradation (TC), and light-induced degradation (LID), as these mechanisms are most severe or occurring most frequently [30,31].

Certain effects, such as hotspots, potential-induced degradation, and soiling, are excluded from this study as they are not compatible with the modeling approach. Hotspots are due to current inhomogeneity within the cells, which can result from partial shading or wafer impurities [32]. However, since the PVMD Toolbox assumes all cells are identical and, in this study, considers an unobstructed horizon, hotspot effects cannot be incorporated into the model. Similarly, PID occurs due to a potential difference between the module frame and the active circuit, which can reach up to 1500 V when multiple modules are connected in series [33]. This phenomenon cannot be captured in the simulations, as the model considers only the direct current (DC) performance of a single module, where such high potential differences are not present. Finally, the effect of soiling [34] has also been excluded from this model, as rainfall is not included as input parameter of the PVMD Toolbox, and cleaning strategies would need to be considered, making it a complex degradation mechanisms to model. It would be interesting for future work, however, to study how soiling impacts the current matching in tandem devices, as soiling effects are not the same across all wavelengths [35]. Nevertheless, the exclusion of these mechanisms does not lead to an underestimation of degradation, as the final calibration is based on real-world outdoor PV system data. Moreover, similar analytical models in the literature [28,29] also do not account for these more complex degradation mechanisms.

Each degradation mechanism is characterized by its stress factors, time profile, and impact on the module. Fig. 1b provides an overview of the degradation mechanisms considered in this study. The stress factors considered in the model are ultraviolet (UV) irradiance, the temperature of the module (T), the relative moisture content (RMC), and the photo-generated current (J_{ph}). Another important characteristic is the time profile of a degradation mode. Degradation rates are not necessarily constant over time; they may increase or decrease throughout the module's lifespan [36], as will be shown later in Fig. 7. Finally, the degradation modes are characterized by which part of the module they affect.

For each mechanism, a separate degradation rate k_i is calculated. To obtain the power loss ($P_{loss,i}$) solely due to a mechanism i, we use

$$P_{loss,i}(t) = \int_0^t k_i(\tau) d\tau. \tag{1}$$

It should be realized that all mechanisms affect the performance differently at the same time. This means that the total P_{loss} does not necessarily equal the sum of the individual power losses.

2.1.1. Discoloration

The encapsulant in PV modules, typically made of ethylene vinyl acetate (EVA) or polyolefin (POE) [37], undergoes color changes over its lifetime. Exposure to UV radiation can alter the encapsulant's chemical composition, impacting the optical performance of the device [38].

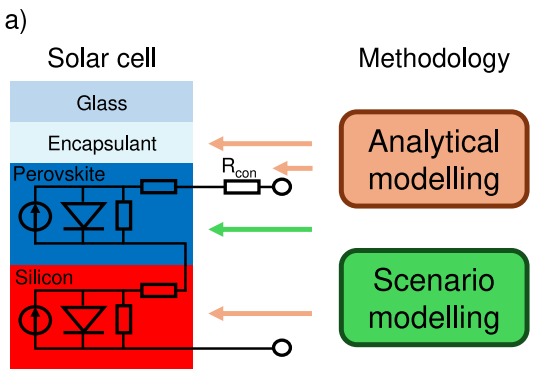

b)

Mechanism	Stress factor	Time profile	Effect on module
Discoloration	UV, T	Constant	Encapsulant
MID	RMC, T	Increase	Bottom cell
TC	T	Decrease	R_{con}
LID	J_{ph}	Decrease	Bottom cell

Fig. 1. (a) An overview of the methodology, where a scenario-based approach is used for degradation in the top cell, and an analytical approach is used for the bottom cell, encapsulant, and contact resistance. (b) An overview of the degradation mechanisms considered for the analytical model, including their stress factors, time profile, and effect on the module. MID, TC, LID, and RMC stand for moisture-induced degradation, thermal cycling, light-induced degradation, and relative moisture content.

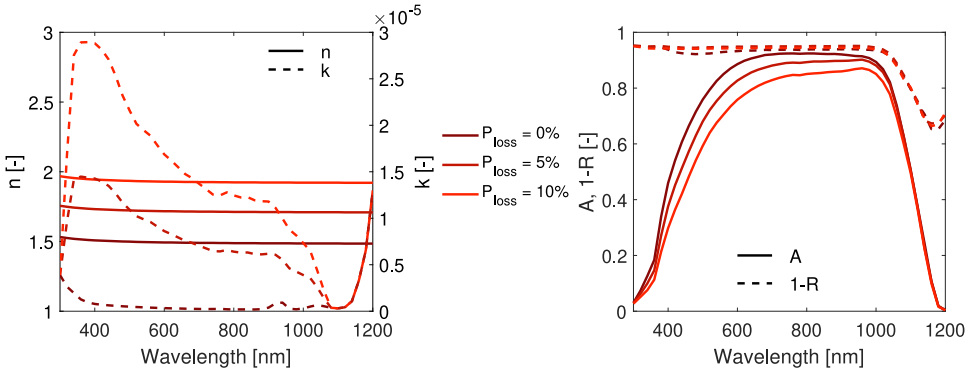

Fig. 2. The change in $N(\lambda)$ and its effect on the absorption profile for different values of P_{loss}, solely due to discoloration.

To predict the performance loss due to discoloration, we use the modified Arrhenius equation from Sinha et al. [39], which calculates the discoloration degradation rate (k_{dis}) as:

$$k_{dis} = A_{dis} \cdot e^{\frac{-E_{a,dis}}{k \cdot T}} \cdot (\mathrm{UV})^{n_{dis}}, \tag{2}$$

where A_{dis}, $E_{a,dis}$, and n_{dis} are the pre-exponential factor, the activation energy, and the exponent related to the discoloration, respectively, and k is the Boltzmann constant. Based on the findings in literature, we assume n_{dis} to be 1 [40] and $E_{a,dis}$ to be 0.39 eV [39]. The value of A_{dis} is determined through calibration later in this section. The amount of UV is defined as all in-plane irradiance with a wavelength smaller than 400 nm [41]. Although the UV and T have seasonal fluctuations, they are approximately similar for all years. Therefore k_{dis} is constant throughout the lifetime of the PV module, being consistent with literature [36].

Since discoloration affects the encapsulant's optical properties, we model performance loss by adjusting the refractive index ($N(\lambda) = n(\lambda) + i \cdot k(\lambda)$) of the encapsulant in the EY simulations. The PVMD Toolbox uses $N(\lambda)$ for each material to calculate the device's optical response [20].

To model changes in the refractive index due to discoloration, we use data from Meena et al. [42], who measured variations in internal quantum efficiency and reflection spectra of discolored modules. The full details of the procedure for calculating $N(\lambda)$ are provided in Appendix B. Fig. 2 illustrates different $N(\lambda)$ for different values of P_{loss} and the corresponding the optical response. This change in optical response will then also have an impact on the thermal and electrical simulation step of the PVMD Toolbox.

2.1.2. Moisture induced degradation

Moisture ingress in PV modules can trigger various degradation modes, such as delamination and corrosion [43,44]. While these mechanisms are distinct, it is challenging to separate them due to their same stress factor. Therefore, their effects are combined in our analysis.

To quantify the amount of degradation due to MID (k_{MID}), the Peck model is used [11,28,29,45]:

$$k_{MID} = A_{MID} \cdot e^{-\frac{E_{a,MID}}{k \cdot T}} \cdot (\mathrm{RMC})^{n_{MID}}, \tag{3}$$

where A_{MID}, $E_{a,MID}$, and n_{MID} are the pre-exponential factor, the activation energy, and the exponent related to MID, respectively. The RMC is the relative moisture content that describes the amount of moisture that has entered the module compared to the saturation concentration of the encapsulant. In previous work, a model has been developed to simulate and predict the RMC over time for different climates [45]. The values for $E_{a,MID}$ and n_{MID} are assumed to be 0.809 eV and 1.87 based on previous work [45], and A_{MID} will be used for calibration. Since moisture ingress is a gradual process, RMC increases over time. As a result, the degradation rate k_{MID} also increases throughout the module's lifetime, consistent with literature findings [36].

As MID affects both the electrical and optical properties of PV modules, its impact is simulated by adjusting the diode model parameters of the c-Si bottom cell. Zhu et al. [46] conducted damp heat tests to measure the effects of moisture ingress on IV curves. They also identified how the parameters of the equivalent circuit model change due to moisture exposure. These trends are used to adjust the simulation of c-Si performance, incorporating the associated performance loss. Fig. 3a illustrates the changes in the IV curve for different values of P_{loss} caused by MID. More information on the calculation of circuit parameters is provided in Appendix C.

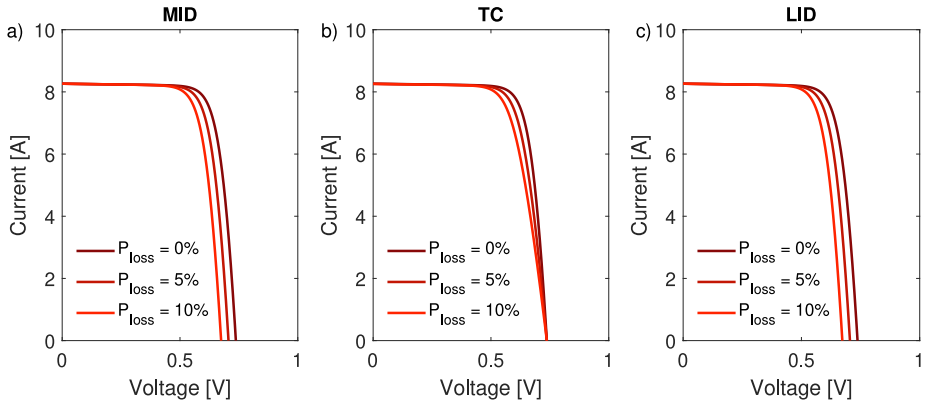

Fig. 3. The effect on the IV curve of different values of P_{loss}, solely due to MID (a), TC (b), and LID (c).

2.1.3. Thermal cycling

In addition to the absolute temperature influencing Arrhenius processes in discoloration and MID, temperature fluctuations over time introduce additional degradation mechanisms. High-temperature variations, combined with mismatches in the thermal expansion coefficients of different materials, cause layers to expand at different rates, leading to thermomechanical stress on the interconnections [47,48]. Bosco et al. [49] proposed an analytical equation that can describe the damage due to TC (D_{TC}), written as

$$D_{TC} = A_{TC} \cdot (\Delta T)^{n_{TC}} \cdot R^b \cdot e^{-\frac{E_{a,TC}}{k \cdot T}}, \tag{4}$$

where A_{TC}, $E_{a,TC}$, and n_{TC} are the pre-exponential factor, the activation energy, and the exponent related to TC, respectively, ΔT is the average daily temperature fluctuation, R is the number of times the temperature has fluctuated, and b is an exponent to R. The values for $E_{a,TC}$, n_{TC}, and b are assumed to be 0.12 eV, 1.9, and 0.33 as calibrated by N. Bosco et al. [49], and A_{TC} will be used for final calibration.

As Eq. (4) outputs the total amount of damage instead of a degradation rate, the degradation rate due to TC (k_{TC}) can be obtained iteratively with

$$k_{TC}(t) = \frac{D_{TC}(t) - \sum_{\tau=1}^{t-1} k_{TC}(\tau) \cdot \Delta t}{\Delta t}, \tag{5}$$

where Δt is the time step. Given that b is equal to 0.33 and R will constantly increase over time, D_{TC} will keep rising but at a slower pace, causing k_{TC} to decrease over time. The time profile of both the damage and k_{TC} and the definition of ΔT are shown in Appendix D. It should be noted that Eq. (5) applies only for $t > 0$. $k_{TC}(0)$ is defined to be 0%/year.

Since TC degradation primarily affects the contacts [47–49], we adjust the value of R_{con} to simulate the required P_{loss}. Fig. 3b illustrates the impact of TC degradation on the IV curve.

2.1.4. Light induced degradation

The final degradation mechanism considered is light-induced degradation (LID), where the efficiency of the solar cell decreases due to prolonged exposure to light. According to literature, this is attributed to an increase in the minority carrier lifetime (τ_{min}) within the solar cell [50–52], with the J_{ph} acting as the stress factor [53,54].

Experimental studies have demonstrated that τ_{min} decays exponentially with exposure to J_{ph} and eventually saturates at a constant value [54,55]. This time-dependent behavior of $\tau_{min}(t)$ can be modeled as:

$$\tau_{min}(t) = \tau_{min,\infty} + (\tau_{min,0} - \tau_{min,\infty}) \cdot e^{\frac{-\int_0^t J_{ph}(\tau) d\tau}{A_{LID}}}, \tag{6}$$

where $\tau_{min,0}$ and $\tau_{min,\infty}$ are the minority carrier lifetime initially and after saturation, and A_{LID} is the decay constant for LID.

Table 1
An overview of the datasets that are used for the calibration and validation of the analytical model, and the calibrated values for the remaining parameters for each parameter set.

Location	Years	Source	A_{dis} [%/y]	A_{MID} [%/y]	A_{TC} [%/y]	A_{LID} [C m^{-2}]
Alice Springs (Australia)	16	DKA [57]	0.0556	1.03×10^8	4.65×10^{-5}	1.23×10^7
Pfaffstäten (Austria)	6	Lindig [58]	1.084	3.72×10^8	9.71×10^{-5}	1.70×10^7
Cocoa (USA)	6	NREL [59]	0.0677	6.10×10^7	1.23×10^{-4}	8.19×10^5
Grimstad (Norway)	20	Segbefia [60]	0.2645	9.61×10^7	2.11×10^{-5}	7.53×10^6
Borlänge (Sweden)	30	Psimopoulos [61]	0.1198	1.92×10^8	4.96×10^{-5}	1.12×10^6

Since τ_{min} and I_0 are inversely proportional [56], the value of I_0 can be adjusted using

$$I_0(t) = \frac{I_{0,init}}{C_\tau(t)}, \tag{7}$$

where $I_{0,init}$ is the initial value of I_0 and $C_\tau(t)$ is the ratio of $\tau_{min}(t)$ over $\tau_{min,0}$, written as

$$C_\tau(t) = \frac{\tau_{min}(t)}{\tau_{min,0}} = C_{\tau,\infty} + (1 - C_{\tau,\infty}) \cdot e^{\frac{-\int_0^t J_{ph}(\tau) d\tau}{A_{LID}}}, \tag{8}$$

where $C_{\tau,\infty}$ is $\frac{\tau_{min,\infty}}{\tau_{min,0}}$. Based on measurements in literature [55], $C_{\tau,\infty}$ is assumed to be 0.5, and A_{LID} is used for calibration. The effect of LID on the IV curve is shown in Fig. 3c.

In contrast to the other degradation mechanisms, there is no direct analytical equation for the degradation rate due to LID ($k_{LID}(t)$). Instead, it can be derived from the change in power output as

$$k_{LID}(t) = \frac{1 - \frac{P(t+\Delta t)}{P(t)}}{\Delta t}, \tag{9}$$

where $P(t)$ is the output power at time t, excluding the other losses.

2.1.5. Calibration and validation

Each degradation mechanism considered has one parameter that can be used to calibrate the models based on outdoor measurements. For this calibration process, we rely on measured outdoor data from various PV systems reported in the literature. Table 1 provides an overview of the datasets selected for this calibration.

For each dataset, the data was filtered and normalized to obtain the normalized power ($P_{norm}(t)$) for each operating year. Full details of the filtering and normalization process are provided in Appendix

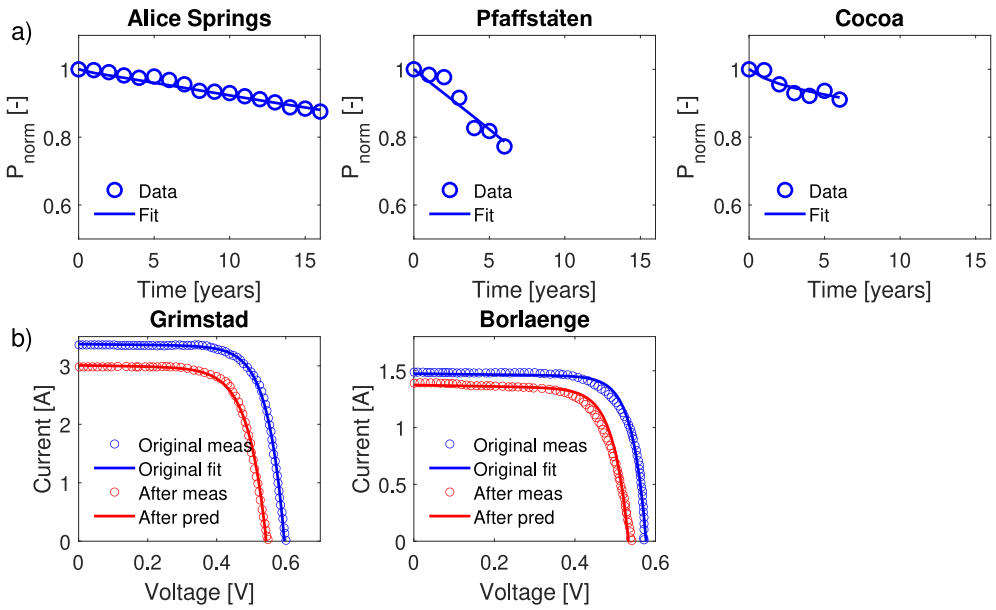

Fig. 4. (a) The calibration and validation of the analytical model for the different datasets. (b) A validation of the analytical model on the effect of degradation on the IV curve.

E. Calibration was performed separately for each dataset, resulting in different values for A_{dis}, A_{MID}, A_{TC}, and A_{LID}. This variation can be attributed to differences in module characteristics, as the degradation parameters are not identical across systems. Fig. 4a shows the calibration results for all datasets, demonstrating that the analytical model accurately captures the temporal trends of P_{norm} for each site.

To further validate the methodology, we assessed its ability to predict changes in the IV curve. Two studies have been found that reported the change in IV curve after 20 or 30 years of operation. Fig. 4b compares the predicted and measured IV curves of both studies, showing that the analytical model successfully captures the loss in IV performance.

The results presented in this work are obtained by using the parameters calibrated with the PV system in Alice Springs. The reason for selecting this dataset is that it has continuously reported the output power of the PV module for the longest time period. To see how using different parameters affect the results, Appendix F shows a sensitivity analysis. This sensitivity analysis contains the result of Fig. 9, obtained with different sets of parameters. It can be seen that the choice of parameter set can significantly change the values of k_{tol}, but the same trends and relative differences are present for all sets.

2.2. Scenario modeling

Degradation in the top cell is simulated using a scenario-based approach. Specifically, we introduce performance loss in the perovskite cell by adjusting parameters in the electrical model, following methods similar to those used by Qian et al. [16] and Orooj et al. [17]. To examine the effect on different degradation trends, three scenarios are considered where there is a loss in short circuit current (I_{sc}), open circuit voltage (V_{oc}), and fill factor (FF). These scenarios are simulated by adjusting I_{ph} (for I_{sc} degradation), I_0 (for V_{oc} degradation), and both R_{sh} as well as R_s (for FF degradation).

It is important to realize that the degradation of a perovskite cell in practice is not a loss in a single component, but rather a combination of multiple losses due to different mechanisms. The reason for analyzing these extreme cases is to establish a range of tolerable degradation rates that encompasses all possible degradation scenarios. If a real-world scenario involves a combination of the tested cases, its tolerable degradation rate will fall somewhere between the values derived in this study.

Fig. 5 illustrates the impact of these scenarios on the IV curve for various values of P_{loss}. To simulate lifetime degradation, different constant values for k_{per} are applied. To indicate a specific degradation scenario, the notation $k_{per,X}$, where X can be I_{sc}, V_{oc} or FF, is used. The corresponding P_{loss} for the top cell is calculated using Eq. (1), enabling the necessary adjustments to the IV curve.

It should be noted that this scenario based approach only considers fixed degradation rates over the lifetime of the PV module. This means that non-linear trend in the degradation of the perovskite cell are not captured by this method.

2.3. Calculating the relative environmental impact

The methodology considered so-far only allows to make comparisons between single junction and tandem devices in terms of energy yield. However, to develop truly sustainable PV modules, it is essential to also consider the environmental impact of both technologies.

To include the environmental impact of both technologies, we use the results from Roffeis et al. [62] who reported the absolute environmental impacts of single-junction c-Si and PerSi tandem modules, covering 13 impact categories listed in Table 2. It should be noted that both modules have the same module area, but a different output power. Interestingly, the PerSi module has a lower environmental impact for the impact category human toxicity and marine ecotoxicity. This is because 37% less silver is used for the metallization process of the PerSi module, as explained by Roffeis et al. The silver reduction is enabled by the fact that tandem modules have about 50% lower currents as compared to Si single junction modules [62].

While these absolute environmental impact values (EI_{abs}) are informative, it is more meaningful to compare their relative environmental impacts (EI_{rel}) by accounting for differences in energy production. We compute EI_{rel} using the formula

$$EI_{rel} = \frac{EI_{abs}}{\text{LEY}}, \tag{10}$$

where LEY is calculated with the methodology described above.

The values for EI_{rel} can be used to assess for which degradation rates tandem modules have a lower environmental impact than single junction devices.

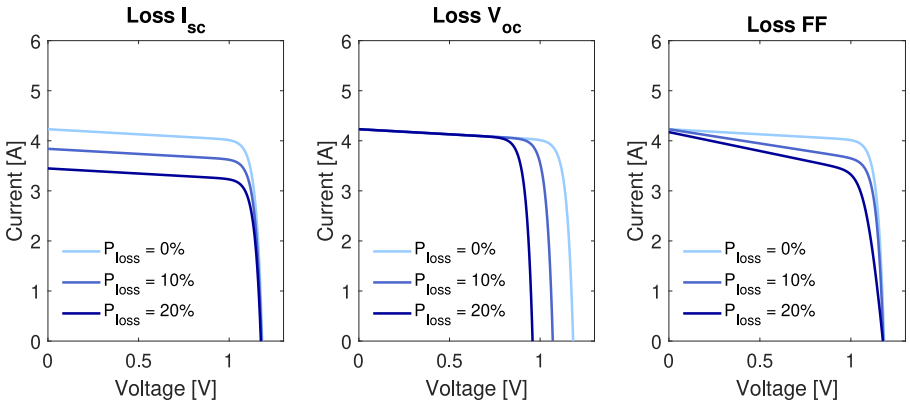

Fig. 5. The effect on the IV curve of the perovskite subcell due to different degradation scenarios.

Table 2
The absolute environmental impact per module in different categories for the c-Si and PerSi tandem module.
Source: These values are obtained from literature [62].

Impact category	Unit	c-Si	PerSi
Climate change, default	kg CO2 eq.	411	434
Particulate matter formc	g PM2.5 eq.	644	684
Fossil depletion	kg oil eq.	157	164
Freshwater consumption	m^3	14	14
Freshwater ecotoxicity	kg 1,4 DB eq.	4	4
Freshwater eutrophication	g P eq.	209	210
Human toxicity, non-cancer	kg 1,4 DB eq.	440	421
Ionizing radiation	kBq Co-60 eq.d	70	71
Marine ecotoxicity	kg 1,4 DB eq.	6	5
Marine eutrophication	g N eq.	29	31
Metal depletion	g Cu eq.	1900	2034
Terrestrial acidification	g SO2 eq.	1510	1577

3. Case studies

The proposed methodology can be used to determine tolerable values for k_{per} of a tandem PV module at different locations using a c-Si PV module as reference. This section outlines the module specifications and the selected geographical locations. For this study only monolithic 2T PerSi modules are considered. The reason for excluding other terminal configurations, such as three- or four-terminal devices, is that there cell and module design is significantly different than the reference c-Si module.

3.1. PV module

The PV module comprises 144 half-cut PerSi tandem cells with a G12 wafer size, connected in butterfly topology with three bypass diodes. The cell design is based on the 32.5% efficient 2T PerSi cell developed by S. Mariotti et al. [63], which has been integrated and validated in the PVMD Toolbox in previous studies [21,22]. Similar to those previous studies, a layer of encapsulant and glass is included to simulate realistic modules. Fig. 6 illustrates the optical structure, absorption profile, and module IV curve for both the reference c-Si as the PerSi module. The module has an output power of 948 W and a total area of 3.38 m^2, meaning the module has a module efficiency of 28.0%.

The reference c-Si module is derived from the bottom cell of the PerSi device shown in Fig. 6. It also consists of 144 half-cut cells with a G12 wafer size, utilizing the same bottom-cell design as the PerSi device.

Both modules consists of monofacial cells, and have a polyethylene terephthalate (PET) backsheet, being similar to modules in previous work [45]. Also, there is an anti-reflection coating (ARC) and an amorphous fluoropolymer (AF) layer on top of the glass to further improve the optical performance.

3.2. Operating conditions

Different geographical locations are selected for which the acceptable values of k_{per} are found. These distinct locations represent different climates according to the Köppen-Geiger-Photovoltaics (KGPV) classification [64,65] and a machine learning based PV climate classification (ML-PV) [66]. Table 3 shows the annual Global Horizontal Irradiance (GHI), weighted average ambient temperature (T_a), average relative humidity (RH), KGPV classification, and the module tilt.

4. Results

We apply the outlined methodology to calculate the Lifetime Energy Yield (LEY) of different modules across four different locations. First, we simulate the performance of the c-Si modules with the analytical model to calculate the modules' lifetime for all locations and their LEY. Next, we calculate the LEY of PerSi modules for all nine scenarios and different values of k_{per}, identifying the maximum tolerable degradation rate. We also factor in the environmental impact of both c-Si and PerSi modules. By considering both energy yield and environmental impact, we determine the values of k_{per} that make PerSi modules more sustainable compared to their c-Si counterparts. Finally, we propose a simplified model that can predict the maximum tolerable degradation rate.

4.1. Reference lifetime energy yield of c-Si modules

To determine the module lifetimes for different locations, we use the analytical model to calculate the degradation rates for all mechanisms. As illustrated in Fig. 7, Lagos exhibits the highest degradation rates due to its high temperatures and humid climate, as indicated in Table 3. Conversely, the modules in Delft demonstrate the longest lifetimes, thanks to the area's lower ambient temperatures. The obtained time profiles of each degradation mechanism align well with the time profiles from literature presented in Fig. 1b.

Based on the simulated degradation rates and the applied methodology, we compute the normalized power (P_{norm}) over time, as depicted in Fig. 7. The module lifetime, defined as the time it takes to reach 80% of the original power output (T_{80}), is also shown on top of the figure. Due to the elevated degradation rates, Lagos has the shortest module lifetime at 13 years. Shanghai and Lisbon follow with similar lifetimes of 26 and 30 years, respectively. Delft, benefitting from its favorable environmental conditions, achieves the longest lifetime of 48 years. It should be noted that similar differences in module lifetime across climates were also found in other studies [28].

The LEY of the modules is calculated by integrating the annual energy yield over time till the module lifetime T_{80}.

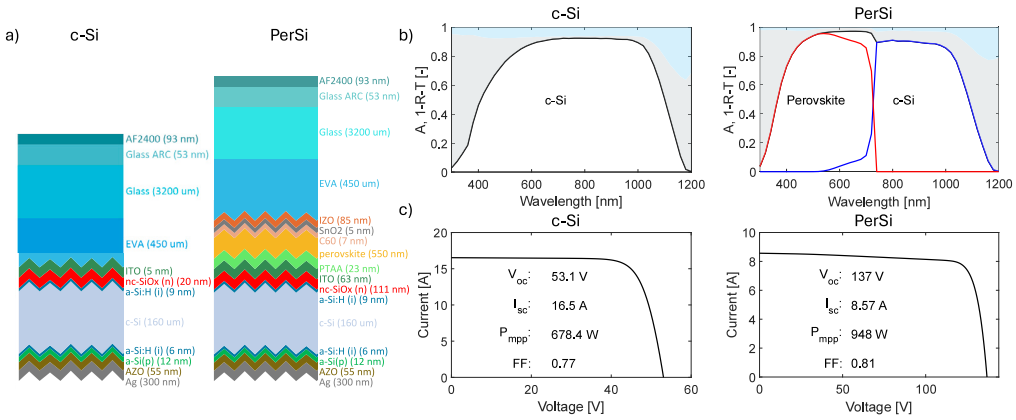

Fig. 6. The optical structure (a), the absorption profile (b), and the IV curve (c) of the simulated PV module.

Table 3
The characteristics of the selected locations. The ambient temperature is weighted with the global horizontal irradiance [21]. This metric is chosen as it, in our opinion, better represents the operating conditions of the PV modules than the normal average of the ambient temperature. The selected module tilts are chosen such that they maximize the annual front-side irradiation for each location. For acronyms in KGPV and ML-PV climates, we refer to [65,66].

Location	Annual global horizontal irradiation [kWh m^{-2}]	Weighted average ambient temperature [°C]	KGPV	ML-PV	Optimal module tilt [°]
Delft	1018	16.2	DL	Tem1	31
Lagos	1642	29.4	AH	Tro2	5
Lisbon	1758	20.6	DH	Tem5	28
Shanghai	1271	21.7	DM	Tro1	17

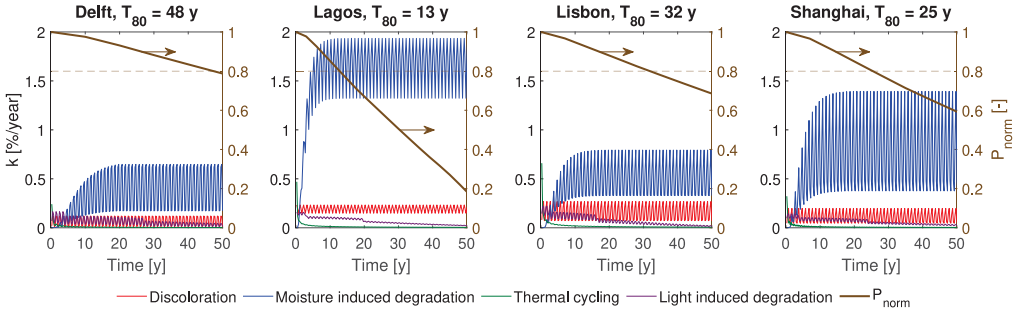

Fig. 7. The degradation rates of the different degradation mechanisms in all locations. Also, the normalized power is plotted such that T_{80} can be determined.

4.2. Tolerable degradation rates

To determine the tolerable value for k_{per}, we employ both the analytical and scenario-based models to calculate the LEY of PerSi modules. For a fair comparison, we use the same module lifetime as calculated for c-Si modules to determine the LEY. As an example, Fig. 8a illustrates the annual EY of the PerSi module in Delft under I_{sc} degradation for different values of k_{per}. As k_{per} increases, the EY declines more rapidly over the module's lifetime due to faster performance degradation.

Fig. 8b integrates the energy production over the module's lifetime to determine the LEY, with the dashed line representing the LEY of c-Si modules. The LEY of PerSi modules decreases as k_{per} increases, indicating a specific threshold value, denoted as k_{tol}. Similar to $k_{per,X}$, $k_{tol,X}$ is used to indicate a specific degradation scenario. This value represents the maximum allowable k_{per} for PerSi devices in order to outperform c-Si modules.

This process is repeated for each location and degradation scenario to calculate k_{tol} under various conditions. Fig. 9 presents the LEY for different values of k_{per} for all PerSi modules, along with the corresponding k_{tol} values. It should be noted that LEY is simulated only for integer values of k_{per} and the intermediate values are found via linear interpolation.

Across all locations, degradation in I_{sc} yields the lowest k_{tol} (1.2% per year for Delft) as two-terminal modules require current matching between subcells. As a result, current losses are more harmful than voltage losses. This also explains why k_{tol} values for FF degradation are lower than those for V_{oc} degradation, as fill factor losses affect both current and voltage.

Another key observation is that k_{tol} is inversely linked to T_{80}. In Delft, where there is a high module lifetime, the perovskite top cell needs to be very stable as a degradation rate of only 1.9% can be tolerated. On the other hand, in Lagos, where the module lifetime is short, a larger perovskite degradation rate of 7.6% can be tolerated. This occurs because the total degradation in the perovskite cell ($k_{tol} \cdot T_{80}$) remains approximately constant across locations. Consequently, locations with lower T_{80} have larger k_{tol} values, as the modules last shorter at that location anyway, meaning perovskite degradation is less of an issue.

4.3. Effect of higher efficiency

The PV module used in the simulations is based on a 32.5% efficient PerSi tandem cell, resulting in a module efficiency (η_{mod}) of 28.0%.

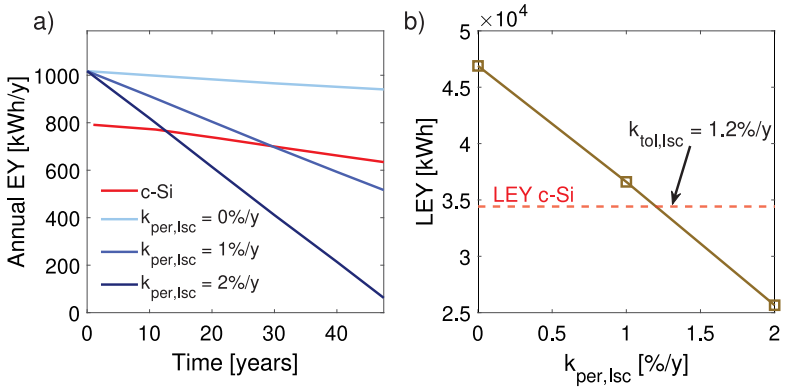

Fig. 8. An example for identifying the tolerable degradation rate $k_{tol,Isc}$ for the modules in Delft. (a) shows the annual EY of the c-Si and PerSi modules for different values of $k_{per,Isc}$. (b) shows the integrated LEY, such that $k_{tol,Isc}$ can be determined for the case of Delft.

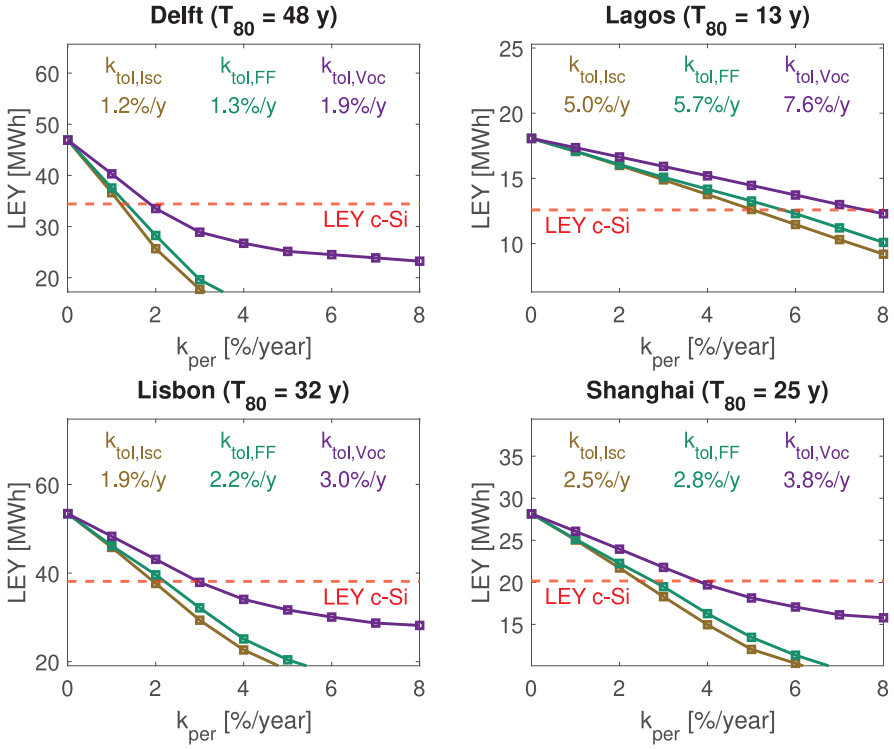

Fig. 9. The LEY for different values of k_{per} and the corresponding k_{tol} for each location and degradation mechanism.

However, (η_{mod}) could be higher, as the practical efficiency limit of PerSi technology is 39.5% [3]. An increase in efficiency would enhance the energy yield (EY) for tandem modules, which could in turn impact k_{tol}.

To explore this effect, we repeat the previously described procedure using modules with higher efficiencies. The performance of the perovskite cell is artificially improved, as illustrated in Fig. 10, achieving a module efficiency of up to 32.9%. Details of these performance enhancements are provided in Appendix G.

The higher-efficiency modules are labeled according to their respective efficiencies. Fig. 11 presents the corresponding k_{tol} values for all modules across different locations and efficiency levels, showing a clear influence of η_{mod} on the tolerable degradation rate.

For instance, in Delft, the k_{tol} for I_{sc} degradation increases from 1.2% to 1.9% per year, representing a relative increase of nearly 50%. This same approximate increase is observed in other locations and degradation scenarios. The highest k_{tol} is found in Lagos for V_{oc} degradation, primarily because lower module lifetimes lead to higher k_{tol}, and voltage degradation is less harmful than current degradation.

Overall, these simulations quantify by how much the tolerable degradation rate under expands with improving module efficiency. This illustrates that higher efficiency not only boosts energy production but can also loosen the stability requirements of the perovskite cell.

As mentioned in Section 2.2, practical degradation scenarios will most likely not be a loss solely in I_{sc}, V_{oc}, or FF, but a combination of them. The presented results can be used to create a window of tolerable degradation rates for the perovskite cell at different module efficiencies, as shown in Fig. 12. As mentioned before, degradation in current is most harmful for 2T tandem cells and degradation in voltage is least harmful, meaning these scenarios function as two extreme scenarios. Therefore, the tolerable degradation rate for any possible scenario is in between $k_{tol,Isc}$ and $k_{tol,Voc}$, indicated with the gray area in Fig. 12. This figure shows what is the minimum and maximum value for k_{tol} at different locations and module efficiencies.

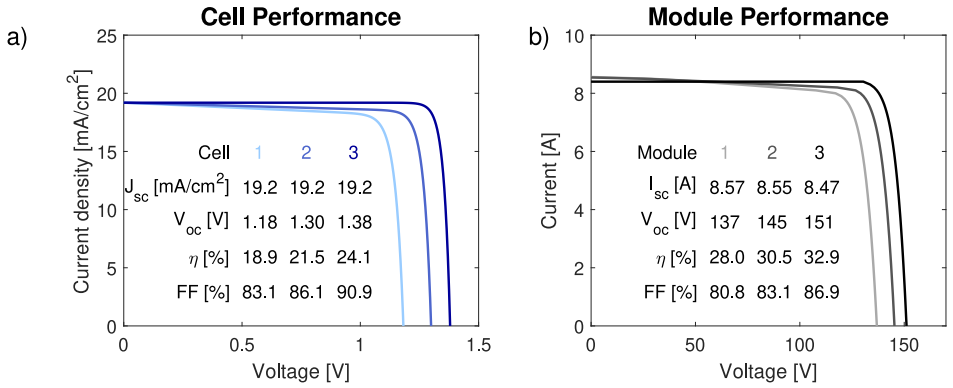

Fig. 10. (a) The cell performance of perovskite subcells with increasing quality. The separate perovskite subcells can reach an efficiency of 24.1%. (b) The module performance with increasing perovskite efficiencies.

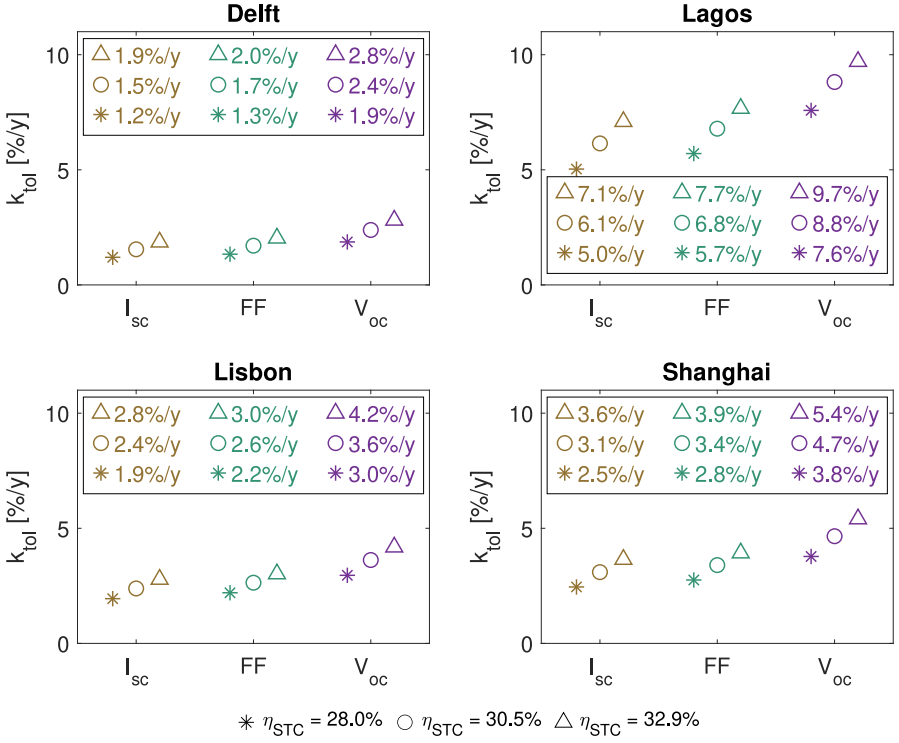

Fig. 11. The effect of the module efficiency on k_{tol}. It can be seen that higher efficient modules have a larger tolerable degradation rate.

In practice, it is more practical to measure the degradation rate of a PerSi module rather than focusing specifically on the top cell. To identify a single tolerable degradation rate for the entire PerSi module, one can use the value of $k_{tol,Isc}$ as an approximation. Since the module consists of two-terminal cells, meaning its current is limited by the lowest subcell, any value of $k_{per,Isc}$ will also translate into a similar module degradation rate.

4.4. Simplified model

The current methodology requires significant computational effort since energy yield must be calculated for each year and for various values of k_{per}. To avoid these computationally-intensive simulations, a more streamlined approach is desirable. Therefore, we explore the potential of developing a simplified model to predict k_{tol}.

Our proposed simplified model is an Arrhenius-based equation written as

$$k_{tol} = c_{sim} \cdot \eta_{mod} \cdot e^{\frac{-E_{a,sim} \cdot q}{k \cdot T_a}}, \tag{11}$$

Table 4
The calibrated values for c_{sim} and $E_{a,sim}$ that are used in the simplified model.

$c_{sim,I_{sc}}$ [y^{-1}]	$c_{sim,FF}$ [y^{-1}]	$c_{sim,V_{oc}}$ [y^{-1}]	$E_{a,sim}$ [eV]
4.71×10^{11}	5.19×10^{11}	6.85×10^{11}	0.743

where c_{sim} is a pre-exponential constant that depends on the degradation type, $E_{a,sim}$ is the activation energy of the simplified model, and T_a is the weighted ambient temperature from Table 3.

Although the physical degradation model accounts for multiple stress factors, the simplified model considers only temperature. This decision avoids the need for additional parameters that would require calibration. Given the limited dataset, including multiple factors could lead to overfitting, making a single-factor model more practical.

The parameters c_{sim} and $E_{a,sim}$ are calibrated using the results from Fig. 11, with the final values shown in Table 4.

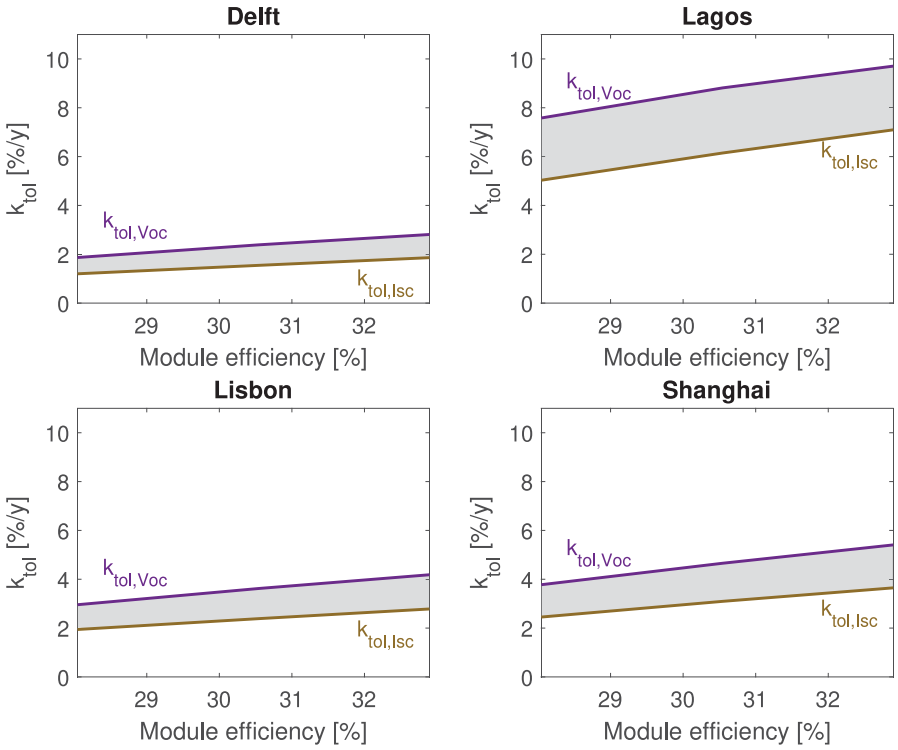

Fig. 12. The window of tolerable degradation rates for the perovskite cell at different module efficiencies.

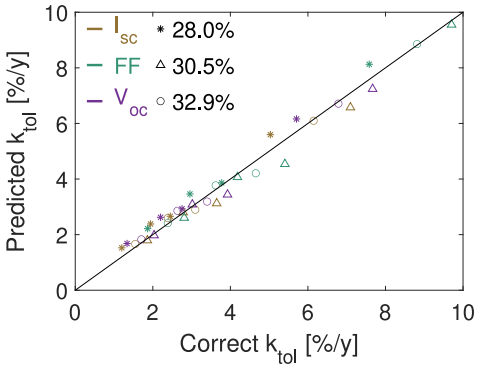

Fig. 13. The comparison between the predicted values for k_{tol} with the simplified model and the simulated values with the detailed methodology.

To assess the accuracy of this approach, we apply the simplified model to predict k_{tol} values for the simulated scenarios. Fig. 13 compares these predicted values with the simulation results. The model performs well, achieving a root mean square error of 0.34% per year. This demonstrates that the simplified model provides accurate predictions for k_{tol} across all degradation scenarios and module efficiencies, making it a reliable tool for predicting k_{tol} under different climate conditions without detailed simulations.

4.5. Including the environmental impact

The values presented for k_{tol} indicate the maximum degradation rate at which PerSi devices achieve a larger LEY than c-Si modules. However, as mentioned before, it is essential to also consider the environmental impact of both technologies to make a good comparison.

We use the approach outlined in Section 2 to identify the perovskite degradation rate at which the relative environmental impact of PerSi modules is lower than that of c-Si modules, denoted with $k_{tol,EI}$. Fig. 14 illustrates $k_{tol,EI}$ across all impact categories and locations for PerSi modules with a 28% efficiency. The first row provides a reference value for k_{tol} when only considering LEY.

In general, $k_{tol,EI}$ values are lower than k_{tol}. This can be attributed to the more complex structure of PerSi cells, which require additional materials and production steps, thereby increasing their environmental footprint. Fig. 14 reflects this, showing a higher absolute environmental impact for PerSi modules despite their higher energy yield. Consequently, when PerSi devices achieve equal LEY to c-Si modules, their environmental impact relative to LEY is higher. Therefore, the tolerable degradation rates for environmental impact are generally lower than the one for LEY ($k_{tol,EI} < k_{tol,EY}$) However, there are exceptions. In the categories Human Marine Ecotoxicity, PerSi devices exhibit lower absolute environmental impacts, resulting in higher $k_{tol,EI}$ values compared to those based solely on LEY.

Overall, the lowest $k_{tol,EI}$ values are approximately 15% to 20% lower than when considering only LEY. This suggests that PerSi modules with degradation rates below these minimum $k_{tol,EI}$ values are more sustainable than c-Si devices across all considered environmental aspects.

5. Conclusion

In this work, we introduced a novel approach for simulating degradation in PerSi tandem modules by combining an analytical model for the bottom cell with a scenario-based model for the top cell. The analytical model was validated using reported performance data from various outdoor PV modules. This methodology enabled us to determine the operational lifetime of c-Si PV modules across four different locations.

We then identified the tolerable degradation rates for the perovskite cell, ensuring that the PerSi module continues to outperform the c-Si module. Various degradation scenarios were analyzed, with degradation in I_{sc} found to be the most critical, resulting in the lowest k_{tol}. Notably, k_{tol} is inversely related to the module's lifetime. In temperate climates where high module lifetimes can be achieved (Delft), the perovskite top cell needs to be very stable as a degradation rate of

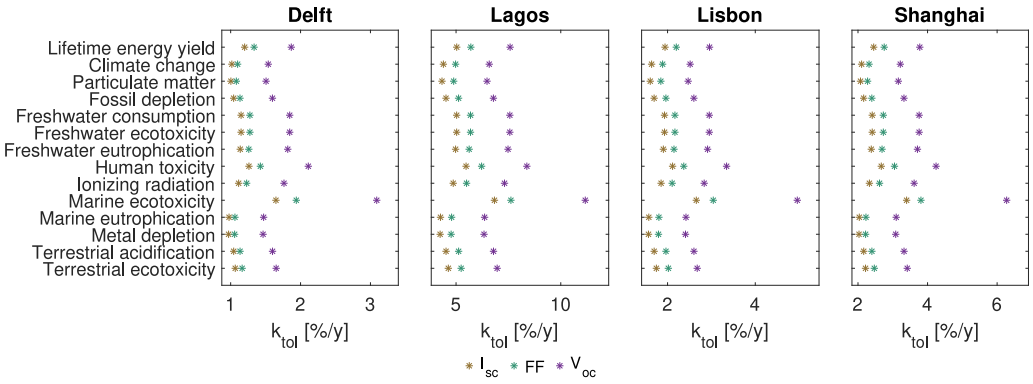

Fig. 14. The values of k_{tol} when considering all environmental impact categories. The first row indicates the original calculate value for k_{tol} when only considering LEY ($k_{tol,EY}$). All results are obtained by using the original PerSi module with an efficiency of 28%.

only 1.9% can be tolerated. On the other hand, in humid/tropical climates (Lagos), where module lifetime anyway is short, a larger perovskite degradation rate of 7.6% can be tolerated. Additionally, we demonstrated that improving module efficiency can relatively increase k_{tol} by nearly 50%.

To avoid the computationally intensive simulations, we introduced a simplified model that can predict the tolerable degradation rate. This Arrhenius-based model considers only module efficiency and ambient temperature. With a root mean square error of 0.34% per year, the model effectively and accurately predicts k_{tol} for different locations, offering a practical alternative for future analyses.

Beyond considering only electricity production, we also factored in the environmental impact. $k_{tol,EI}$ was calculated for different environmental categories, showing that using approximately 80% of the calculated k_{tol} from LEY ensures that PerSi modules are more sustainable across all aspects.

CRediT authorship contribution statement

Youri Blom: Writing – original draft, Methodology, Investigation. **Rudi Santbergen:** Writing – review & editing, Supervision. **Olindo Isabella:** Writing – review & editing, Supervision. **Malte Ruben Vogt:** Writing – review & editing, Supervision, Methodology, Investigation.

Declaration of Generative AI and AI-assisted technologies in the writing process

During the preparation of this work the author used Copilot in order to paraphrase sentences and improve the language and readability. After using this tool/service, the author reviewed and edited the content as needed and takes full responsibility for the content of the publication.

Funding

This research did not receive any specific grant from funding agencies in the public, commercial, or not-for-profit sectors.

Declaration of competing interest

The authors declare that they have no known competing financial interests or personal relationships that could have appeared to influence the work reported in this paper.

Appendix A. Limitation of single degradation value in a tandem device

As mentioned in the main text, the type of degradation (current or voltage loss) in a subcell influences the overall power loss (P_{loss}) differently. Fig. A.1 illustrates that a 10% current loss in the perovskite subcell results in an 8.7% power loss, while a 10% voltage loss leads to a 6.2% power loss. This shows that the degradation in both the perovskite and silicon subcell is relevant, and a single value for k is not sufficient.

Appendix B. Calculating changes in $N(\lambda)$ due to discoloration

To model the effect of discoloration, we adjust the refractive index ($n(\lambda) + i \cdot k(\lambda)$) of the encapsulant layer via

$$\begin{aligned} n_{new}(\lambda) &= n_{orig}(\lambda) + \Delta n(\lambda) \\ k_{new}(\lambda) &= k_{orig}(\lambda) + \Delta k(\lambda), \end{aligned} \tag{B.1}$$

where $\Delta n(\lambda)$ and $\Delta k(\lambda)$ are the changes in refractive index. In order to calculate $\Delta n(\lambda)$ and $\Delta k(\lambda)$, we use the work of Meena et al. [42], who reported external quantum efficiency (EQE) and the reflection of field aged modules, as shown in Fig. B.1.

We begin by computing the change in parasitic absorption across all wavelengths. The spectral parasitic absorption ($A_{par}(\lambda)$) accounts for photons absorbed without contributing to current generation and is defined as $A_{par}(\lambda) = 1 - R(\lambda) - EQE(\lambda)$. $A_{par}(\lambda)$ is calculated for both reference and field-aged modules, allowing us to obtain the difference in parasitic absorption ($\Delta A_{par}(\lambda)$). To control the degradation level, we introduce a parameter c_{dis}, which scales $\Delta A_{par}(\lambda)$.

We make the assumption that this additional parasitic absorption is only absorbed in the encapsulant. By using the Lambert–Beer law, we find the difference in absorption coefficient $\Delta\alpha(\lambda)$ via

$$(1 - R(\lambda)) \cdot e^{-\Delta\alpha(\lambda) \cdot d_{EVA}} = \left(1 - R(\lambda) - c_{dis} \cdot \Delta A_{par}(\lambda)\right), \tag{B.2}$$

where d_{EVA} is the thickness of the EVA encapsulant. Rearranging Eq. (B.2) provides an explicit function for $\Delta\alpha(\lambda)$, written as

$$\Delta\alpha(\lambda) = -\ln\left(\frac{1 - R(\lambda) - c_{dis} \cdot \Delta A_{par}(\lambda)}{1 - R(\lambda)}\right) / d_{EVA} \tag{B.3}$$

We can obtain $\Delta k(\lambda)$ via

$$\Delta k(\lambda) = \frac{\Delta\alpha(\lambda) \cdot \lambda}{4\pi} \tag{B.4}$$

To determine $n_{new}(\lambda)$, we assume $\Delta n(\lambda)$ is approximately equal to c_{dis}, such that only one changing variable is needed. This assumption is justified by the fact that n and k are connected via the Kramers–Kronig (KK) relationship [67]. Numerical KK integration [68] of $\Delta k(\lambda)$ confirms that $\Delta n(\lambda)$ is nearly constant.

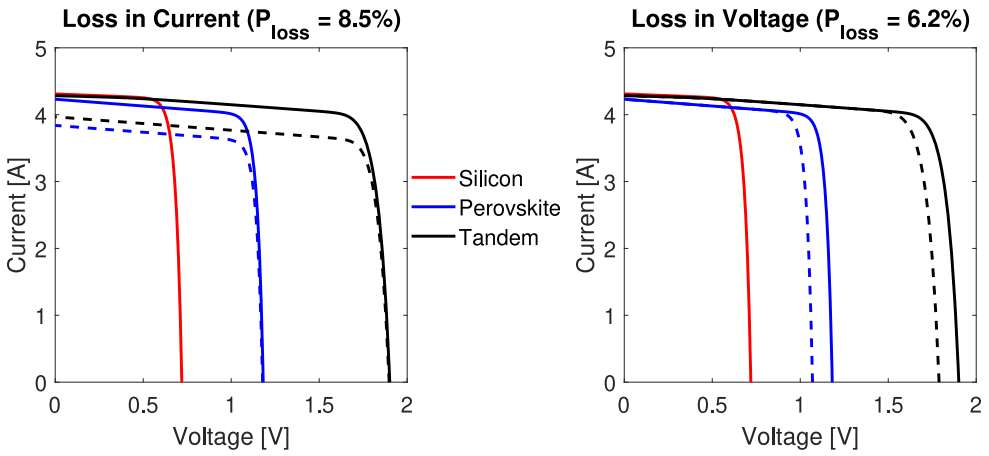

Fig. A.1. The effect of a 10% current (left) or voltage (right) loss in the perovskite subcell (blue) on the loss on 2 terminal tandem IV curve (green). The solid and dashed lines represent the original and degradated IV curves, respectively. It can be seen that a loss in voltage has a lower impact than a loss in current.

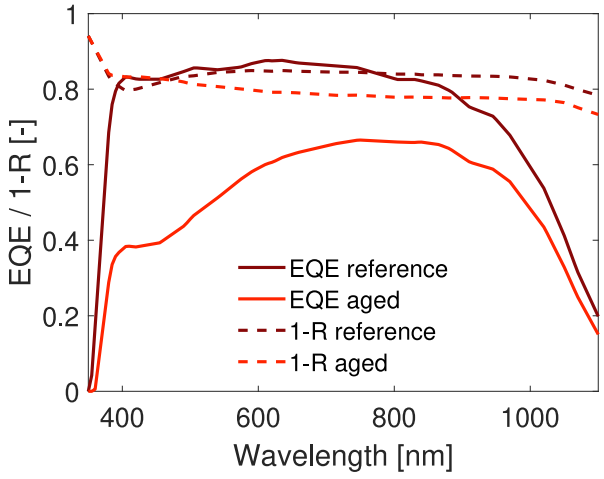

Fig. B.1. The change in EQE and reflection due to discoloration.
Source: The data is obtained from literature [42].

To connect c_{dis} to P_{loss} due to discoloration, we simulate the optical absorption for different values of c_{dis} and calculate the loss in current. Fig. B.2a illustrates the effect of c_{dis} on the absorption profile of the solar cell. It can be seen that there is a similar trend compared to the original measurements in Fig. B.1. Fig. B.2b demonstrates how c_{dis} affects the current loss, providing a basis for selecting appropriate c_{dis} values for specific degradation levels.

Appendix C. Calculating changes in circuit parameters due to MID

To model the impact of moisture ingress on the IV curve of a silicon solar cell, we base our approach on the work of Zhu et al. [46], who provided circuit parameter values under varying stress levels quantified in a procedure-defined unit (p.d.u.) [46].

First, we extracted the trends for each circuit parameter from the experimental data and applied these trends to our c-Si cell. Fig. C.1a illustrates the variation of circuit parameters with different stress doses, while Fig. C.1b shows the corresponding power loss.

To model the power loss caused by moisture ingress, we use Eq. (3) to predict the required power loss and identify the associated dose value. This dose value enabled us to determine the degraded circuit parameter values.

Appendix D. Time profile of thermal cycling

The effect of thermal cycling is modeled by using the equation from Bosco et al. [49]. This equation describes the amount of damage experienced by the PV module as a function of temperature fluctuation ΔT. For this work, we define ΔT to be the average of the daily temperature fluctuation, written as

$$\Delta T = \frac{\sum_{i=1}^{N_{days}} \left(\max(T_i) - \min(T_i)\right)}{N}_{days}, \tag{D.1}$$

where N_{days} is the number of days in the year, and T_i is the temperature at day i. The damage due to thermal cycling is then translated into a degradation rate k_{TC} via Eq. (5). Fig. D.1 shows the time profile of the damage and degradation rate over time for the c-Si module in Delft.

Appendix E. Filtering and normalization datasets

The datasets summarized in Table 1 provide performance measurements of PV systems over several years. To obtain P_{norm}, we have preformed the following steps.

First, a data filtering process was conducted. Data points with GHI values below 200 $\mathrm{W\,m^{-2}}$ or above 1200 $\mathrm{W\,m^{-2}}$ were excluded. Additionally, only measurements recorded at 12:00 were selected to ensure consistent solar positioning across all data points.

The power output was then normalized to standard test conditions (STC) using an equation from literature [11,69]

$$P_{norm} = P_{ac} \cdot \frac{G_{STC}}{GHI} \cdot \frac{1}{1 + \gamma \cdot \left(T - T_{STC}\right)}, \tag{E.1}$$

where P_{ac} is the provided output power, G_{STC} and T_{STC} are the irradiance-level and temperature at STC (i.e. 1000 $\mathrm{W\,m^{-2}}$ and 25 °C, respectively), and γ is the temperature coefficient.

Following normalization, outliers were removed by excluding data points with deviations exceeding twice the standard deviation. Finally, the data were averaged over 100 samples to smooth variations and enhance the visibility of trends.

Appendix F. Sensitivity analysis for parameters in physical model

As mentioned in the main text, the parameters for the physical model are based on the calibration performed for the PV system in Alice Springs. To see how different parameters would change the results, we repeat the calculations for the tolerable degradation rates with different parameter sets. Table 1 contains the parameters for PV modules from all five datasets that can be used for a sensitivity analysis.

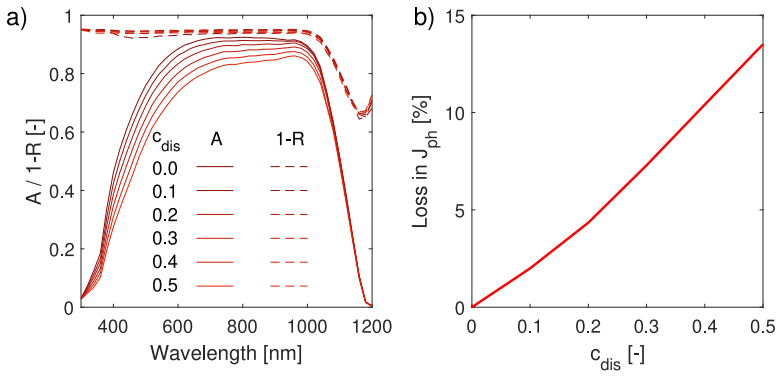

Fig. B.2. The effect of c_{dis} on the absorption and reflection profiles (a) and the loss in current (b).

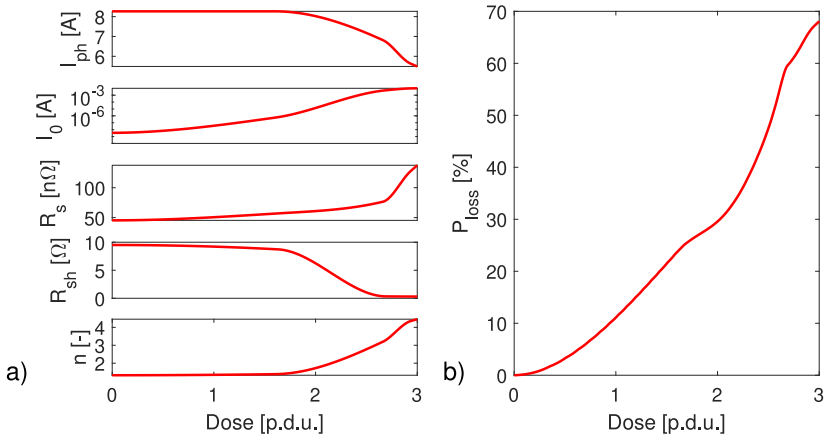

Fig. C.1. The effect of moisture ingress dosage on the circuit parameters (a) and the power loss (b).

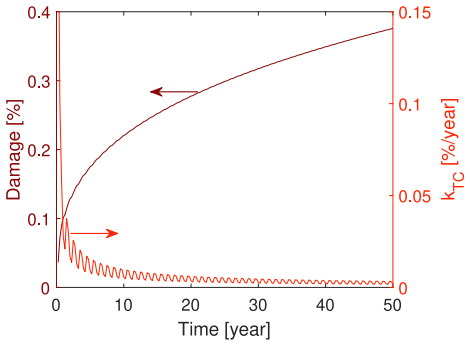

Fig. D.1. The time profile of the damage and the degradation rate due to thermal cycling.

The parameter set for Pfaffstäten has been excluded, as a normalized power of 0.8 was already reached after 5 years, being much smaller than typical module lifetimes.

It is important to note that the differences between the datasets are not only due to varying locations but also to differences in PV modules and their respective systems. Since each module uses a distinct bill of materials and manufacturing process, their degradation rates can vary, explaining the differences observed in parameter values.

Fig. F.1 shows how the tolerable degradation rate changes when different parameter sets are used. It can be seen that the parameters can have a significant impact on the tolerable degradation rates. This is because the parameters impact the degradation rates of the physical model, which affect the value of T_{80}. Since the product $k_{tol} \cdot T_{80}$, stays approximately constant, as mentioned in the main text, the tolerable degradation rates change accordingly.

For all simulated locations, it can be seen that k_{tol} is the lowest when the parameters are calibrated for Cocoa PV module dataset, as the these calibrated values are, extend A_{dis} the lowest for all datasets (Table 1). This results in a larger module lifetime, leading to lower values for k_{tol}. Similarly, k_{tol} is the largest when the Boränge PV module dataset is used, as the parameters in this calibration are the largest.

Overall, it can be seen that for each parameter set, the same trends and relative differences among locations and degradation scenarios are visible.

Appendix G. Improving the perovskite quality

Fig. 10a illustrates the IV curves of perovskite subcells with enhanced efficiencies. To simulate these higher-quality subcells, new calibrated lumped element method (CLEM) models are made. The full details for how the CLEM model is constructed are explained in previous literature [20]. To make the new CLEM models, the electrical parameters are adjusted. Each parameter is interpolated between its original value and the corresponding value for an ideal solar cell, using a factor denoted as c_{per}. This factor ranges from 0 to 1, where $c_{per} = 0$ represents the original cell configuration, and $c_{per} = 1$ corresponds to the ideal cell.

Based on the value of c_{per}, the value of the electrical circuit parameters are determined by

$$\begin{aligned} I_0 &= \exp\left(\log(I_{0,orig}) \cdot (1 - c_{per}) + \log(I_{0,ideal}) \cdot c_{per}\right) \\ n &= n_{orig} \cdot (1 - c_{per}) + n_{ideal} \cdot c_{per} \\ R_s &= R_{s,orig} \cdot (1 - c_{per}) + R_{s,ideal} \cdot c_{per} \\ \frac{1}{R_{sh}} &= \frac{1}{R_{sh,orig}} \cdot (1 - c_{per}) + \frac{1}{R_{sh,ideal}} \cdot c_{per}, \end{aligned} \tag{G.1}$$

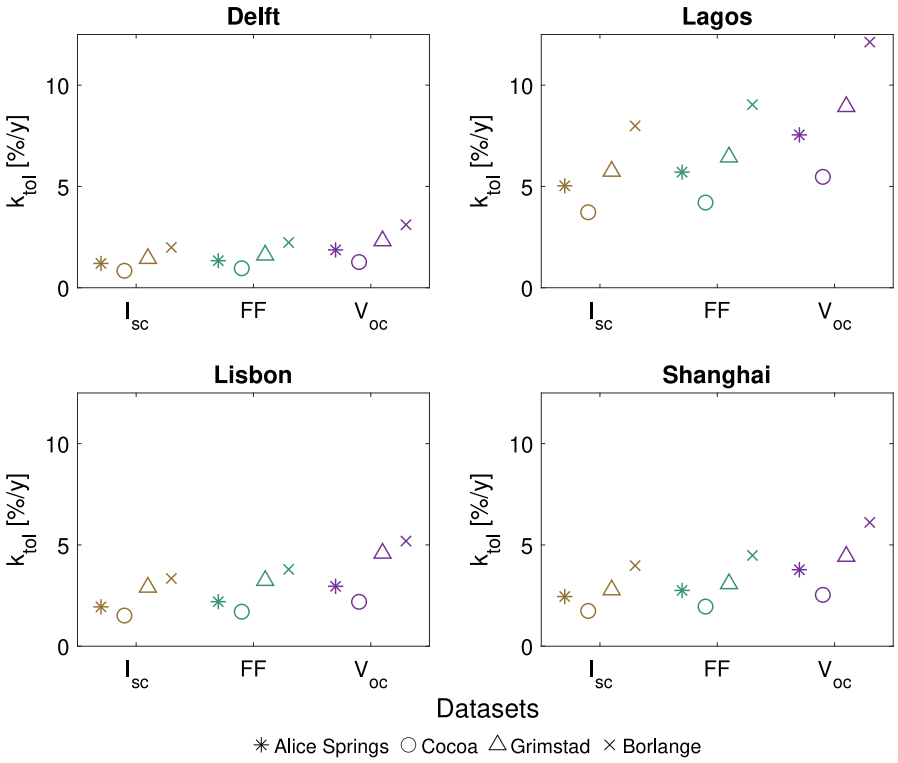

Fig. F.1. A sensitivity analysis of the tolerable degradation rates. The different parameter sets used for the validation are utilized to plot the tolerable degradation rates for the different parameters.

where $n_{ideal} = 1$, and $R_{s,ideal}$ and $R_{sh,ideal}$ are $1 \cdot 10^{-6}$ and $1 \cdot 10^{6}$, respectively, representing arbitrary small and large values. $I_{0,ideal}$ is calculated by using the generalized equation for black body radiation [70]

$$I_{0,ideal} = A_{cell} \cdot \int_0^{\lambda_g} \frac{4\pi \cdot c}{\lambda^4} \cdot \frac{1}{\exp(\frac{h \cdot c}{\lambda \cdot k_b \cdot T}) - 1} d\lambda, \tag{G.2}$$

where c and h are the speed of light and planks constant, respectively, and λ_g is the wavelength corresponding to the perovskite bandgap energy.

In the main text, the two extreme cases are considered, (i.e. $c_{per} = 0$ and $c_{per} = 1$). Additionally, an intermediate scenario is evaluated where c_{per} represents a value such that the subcell efficiency lies halfway between the two extremes. This intermediate value of c_{per} is different for the various IV curves that are needed as input for the CLEM model.

Appendix H. Supplementary data

Supplementary material related to this article can be found online at https://doi.org/10.1016/j.solmat.2026.114169.

Data availability

Other underlying data will be made available on request.

References

[1] A. Richter, M. Hermle, S.W. Glunz, Reassessment of the limiting efficiency for crystalline silicon solar cells, IEEE J. Photovol. 3 (4) (2013) 1184–1191, http://dx.doi.org/10.1109/JPHOTOV.2013.2270351.

[2] S. Schafer, R. Brendel, Accurate calculation of the absorptance enhances efficiency limit of crystalline silicon solar cells with lambertian light trapping, IEEE J. Photovol. 8 (4) (2018) 1156–1158, http://dx.doi.org/10.1109/JPHOTOV.2018.2824024.

[3] O. Er-raji, C. Messmer, A.J. Bett, O. Fischer, S.K. Reichmuth, F. Schindler, M. Bivour, O. Schultz-Wittmann, J. Borchert, M. Hermle, J. Schön, F.D. Heinz, M.C. Schubert, P.S.C. Schulze, S.W. Glunz, Loss analysis of fully-textured perovskite silicon tandem solar cells: Characterization methods and simulation toward the practical efficiency potential, Sol. RRL 7 (24) (2023) http://dx.doi.org/10.1002/solr.202300659.

[4] A.D. Vos, Detailed balance limit of the efficiency of tandem solar cells, J. Phys. D: Appl. Phys. 13 (5) (1980) 839–846, http://dx.doi.org/10.1088/0022-3727/13/5/018.

[5] Y. Blom, M.R. Vogt, C.M. Ruiz Tobon, R. Santbergen, M. Zeman, O. Isabella, Energy loss analysis of two-terminal tandem PV systems under realistic operating conditions—Revealing the importance of fill factor gains, Sol. RRL 7 (8) (2023) 2200579, http://dx.doi.org/10.1002/solr.202200579.

[6] 34.6%! record-breaker LONGi once again sets a new world efficiency for silicon-perovskite tandem solar cells, 2024, URL https://www.longi.com/en/news/2024-snec-silicon-perovskite-tandem-solar-cells-new-world-efficiency/.

[7] H. Zhu, S. Teale, M.N. Lintangpradipto, S. Mahesh, B. Chen, M.D. McGehee, E.H. Sargent, O.M. Bakr, Long-term operating stability in perovskite photovoltaics, Nat. Rev. Mater. 8 (9) (2023) 569–586, http://dx.doi.org/10.1038/s41578-023-00582-w.

[8] L. Duan, D. Walter, N. Chang, J. Bullock, D. Kang, S.P. Phang, K. Weber, T. White, D. Macdonald, K. Catchpole, H. Shen, Stability challenges for the commercialization of perovskite–silicon tandem solar cells, Nat. Rev. Mater. 8 (4) (2023) 261–281, http://dx.doi.org/10.1038/s41578-022-00521-1.

[9] J. Peng, L. Lu, H. Yang, Review on life cycle assessment of energy payback and greenhouse gas emission of solar photovoltaic systems, Renew. Sustain. Energy Rev. 19 (2013) 255–274, http://dx.doi.org/10.1016/j.rser.2012.11.035, URL https://www.sciencedirect.com/science/article/pii/S1364032112006478.

[10] I. Kaaya, J. Ascencio-Vásquez, K.-A. Weiss, M. Topič, Assessment of uncertainties and variations in PV modules degradation rates and lifetime predictions using physical models, Sol. Energy 218 (2021) 354–367, http://dx.doi.org/10.1016/j.solener.2021.01.071, URL https://www.sciencedirect.com/science/article/pii/S0038092X21000979.

[11] S. Lindig, I. Kaaya, K.-A. Weiss, D. Moser, M. Topic, Review of statistical and analytical degradation models for photovoltaic modules and systems as well as related improvements, IEEE J. Photovol. 8 (6) (2018) 1773–1786, http://dx.doi.org/10.1109/JPHOTOV.2018.2870532.

[12] M. Babics, M. De Bastiani, E. Ugur, L. Xu, H. Bristow, F. Toniolo, W. Raja, A.S. Subbiah, J. Liu, L.V. Torres Merino, E. Aydin, S. Sarwade, T.G. Allen, A. Razzaq, N. Wehbe, M.F. Salvador, S. De Wolf, One-year outdoor operation of monolithic perovskite/silicon tandem solar cells, Cell Rep. Phys. Sci. 4 (2) (2023) 101280, http://dx.doi.org/10.1016/j.xcrp.2023.101280, URL https://www.sciencedirect.com/science/article/pii/S2666386423000395.

[13] M. Remec, Š. Tomšič, M. Khenkin, Q. Emery, J. Li, F. Scheler, B. Glažar, M. Jankovec, M. Jošt, E. Unger, S. Albrecht, R. Schlatmann, B. Lipovšek, C. Ulbrich, M. Topič, From sunrise to sunset: Unraveling metastability in perovskite solar cells by coupled outdoor testing and energy yield modelling, Adv. Energy Mater. 14 (29) (2024) 2304452, http://dx.doi.org/10.1002/aenm.202304452.

[14] M. De Bastiani, E. Van Kerschaver, Q. Jeangros, A. Ur Rehman, E. Aydin, F.H. Isikgor, A.J. Mirabelli, M. Babics, J. Liu, S. Zhumagali, E. Ugur, G.T. Harrison, T.G. Allen, B. Chen, Y. Hou, S. Shikin, E.H. Sargent, C. Ballif, M. Salvador, S. De Wolf, Toward stable monolithic perovskite/silicon tandem photovoltaics: A six-month outdoor performance study in a hot and humid climate, ACS Energy Lett. 6 (8) (2021) 2944–2951, http://dx.doi.org/10.1021/acsenergylett.1c01018, arXiv:https://doi.org/10.1021/acsenergylett.1c01018.

[15] J. Liu, E. Aydin, J. Yin, M. De Bastiani, F.H. Isikgor, A.U. Rehman, E. Yengel, E. Ugur, G.T. Harrison, M. Wang, Y. Gao, J.I. Khan, M. Babics, T.G. Allen, A.S. Subbiah, K. Zhu, X. Zheng, W. Yan, F. Xu, M.F. Salvador, O.M. Bakr, T.D. Anthopoulos, M. Lanza, O.F. Mohammed, F. Laquai, S. De Wolf, 28.2%-Efficient, outdoor-stable perovskite/silicon tandem solar cell, Joule 5 (12) (2021) 3169–3186, http://dx.doi.org/10.1016/j.joule.2021.11.003.

[16] J. Qian, M. Ernst, N. Wu, A. Blakers, Impact of perovskite solar cell degradation on the lifetime energy yield and economic viability of perovskite/silicon tandem modules, Sustain. Energy & Fuels 3 (6) (2019) 1439–1447, http://dx.doi.org/10.1039/C9SE00143C.

[17] S. Orooji, U.W. Paetzold, Energy yield modeling of perovskite–silicon tandem photovoltaics: Degradation and total lifetime energy yield, Energy Technol. 12 (11) (2024) 2400998, http://dx.doi.org/10.1002/ente.202400998, arXiv:https://onlinelibrary.wiley.com/doi/pdf/10.1002/ente.202400998. URL https://onlinelibrary.wiley.com/doi/abs/10.1002/ente.202400998.

[18] E. Aydin, T.G. Allen, M.D. Bastiani, A. Razzaq, L. Xu, E. Ugur, J. Liu, S.D. Wolf, Pathways toward commercial perovskite/silicon tandem photovoltaics, Science 383 (6679) (2024) eadh3849, http://dx.doi.org/10.1126/science.adh3849, URL https://www.science.org/doi/abs/10.1126/science.adh3849.

[19] D.C. Jordan, S.R. Kurtz, K. VanSant, J. Newmiller, Compendium of photovoltaic degradation rates, Prog. Photovolt., Res. Appl. 24 (7) (2016) 978–989, http://dx.doi.org/10.1002/pip.2744.

[20] M. Vogt, C.R. Tobon, A. Alcañiz, P. Procel, Y. Blom, A.N. El Din, T. Stark, Z. Wang, E.G. Goma, J. Etxebarria, H. Ziar, M. Zeman, R. Santbergen, O. Isabella, Introducing a comprehensive physics-based modelling framework for tandem and other PV systems, Sol. Energy Mater. Sol. Cells 247 (2022) 111944, http://dx.doi.org/10.1016/j.solmat.2022.111944.

[21] Y. Blom, M.R. Vogt, O. Isabella, R. Santbergen, Optimization of the perovskite cell in a bifacial two-terminal perovskite/silicon tandem module, Sol. Energy Mater. Sol. Cells 282 (2025) 113431, http://dx.doi.org/10.1016/j.solmat.2025.113431, URL https://www.sciencedirect.com/science/article/pii/S0927024825000327.

[22] Y. Blom, M. Ruben Vogt, H. Uzu, G. Koizumi, K. Yamamoto, O. Isabella, R. Santbergen, Exploring the potential of perovskite/perovskite/silicon triple-junction pv modules in two- and four-terminal configuration, Sol. RRL 9 (2025).

[23] Y. Blom, W. Suprayogi, M. Ruben Vogt, O. Isabella, R. Santbergen, Comparison on module performance and degradation robustness of two-, three-, and four-terminal perovskite silicon configurations under realistic operating conditions, n/a, 2025,

[24] T. Ma, Z. Guo, L. Shen, X. Liu, Z. Chen, Y. Zhou, X. Zhang, Performance modelling of photovoltaic modules under actual operating conditions considering loss mechanism and energy distribution, Appl. Energy 298 (2021) 117205, http://dx.doi.org/10.1016/j.apenergy.2021.117205, URL https://www.sciencedirect.com/science/article/pii/S0306261921006292.

[25] T. Ma, H. Yang, L. Lu, Development of a model to simulate the performance characteristics of crystalline silicon photovoltaic modules/strings/arrays, Sol. Energy 100 (2014) 31–41, http://dx.doi.org/10.1016/j.solener.2013.12.003, URL https://www.sciencedirect.com/science/article/pii/S0038092X13005203.

[26] A. Chouder, S. Silvestre, B. Taghezouit, E. Karatepe, Monitoring, modelling and simulation of PV systems using LabVIEW, Sol. Energy 91 (2013) 337–349, http://dx.doi.org/10.1016/j.solener.2012.09.016, URL https://www.sciencedirect.com/science/article/pii/S0038092X12003416.

[27] K. Ramalingam, C. Indulkar, Solar energy and photovoltaic technology, Distrib. Gener. Syst. (2017) 69–147.

[28] I. Kaaya, M. Koehl, A.P. Mehilli, S. de Cardona Mariano, K.A. Weiss, Modeling outdoor service lifetime prediction of PV modules: Effects of combined climatic stressors on PV module power degradation, IEEE J. Photovol. 9 (4) (2019) 1105–1112, http://dx.doi.org/10.1109/JPHOTOV.2019.2916197.

[29] A. Bala Subramaniyan, R. Pan, J. Kuitche, G. TamizhMani, Quantification of environmental effects on PV module degradation: A physics-based data-driven modeling method, IEEE J. Photovol. 8 (5) (2018) 1289–1296, http://dx.doi.org/10.1109/JPHOTOV.2018.2850527.

[30] D.C. Jordan, T.J. Silverman, J.H. Wohlgemuth, S.R. Kurtz, K.T. VanSant, Photovoltaic failure and degradation modes, Prog. Photovolt., Res. Appl. 25 (4) (2017) 318–326, http://dx.doi.org/10.1002/pip.2866, arXiv:https://onlinelibrary.wiley.com/doi/pdf/10.1002/pip.2866. URL https://onlinelibrary.wiley.com/doi/abs/10.1002/pip.2866.

[31] M. Köntges, S. Kurtz, C. Packard, U. Jahn, K.A. Berger, K. Kato, T. Friesen, H. Liu, M. Van Iseghem, Review of Failures of Photovoltaic Modules, Tech. rep., INTERNATIONAL ENERGY AGENCY, 2014.

[32] M. Simon, E.L. Meyer, Detection and analysis of hot-spot formation in solar cells, Sol. Energy Mater. Sol. Cells 94 (2) (2010) 106–113, http://dx.doi.org/10.1016/j.solmat.2009.09.016, URL https://www.sciencedirect.com/science/article/pii/S0927024809003420.

[33] W. Luo, Y.S. Khoo, P. Hacke, V. Naumann, D. Lausch, S.P. Harvey, J.P. Singh, J. Chai, Y. Wang, A.G. Aberle, S. Ramakrishna, Potential-induced degradation in photovoltaic modules: A critical review, Energy Env. Sci. 10 (2017) 43–68, http://dx.doi.org/10.1039/C6EE02271E.

[34] P. Borah, L. Micheli, N. Sarmah, Analysis of soiling loss in photovoltaic modules: A review of the impact of atmospheric parameters, soil properties, and mitigation approaches, Sustainability 15 (24) (2023) http://dx.doi.org/10.3390/su152416669, URL https://www.mdpi.com/2071-1050/15/24/16669.

[35] J.J. John, V. Rajasekar, S. Boppana, S. Chattopadhyay, A. Kottantharayil, G. TamizhMani, Quantification and modeling of spectral and angular losses of naturally soiled PV modules, IEEE J. Photovol. 5 (6) (2015) 1727–1734, http://dx.doi.org/10.1109/JPHOTOV.2015.2463745.

[36] D.C. Jordan, T.J. Silverman, B. Sekulic, S.R. Kurtz, PV degradation curves: Non-linearities and failure modes, Prog. Photovolt., Res. Appl. 25 (7) (2017) 583–591, http://dx.doi.org/10.1002/pip.2835, arXiv:https://onlinelibrary.wiley.com/doi/pdf/10.1002/pip.2835. URL https://onlinelibrary.wiley.com/doi/abs/10.1002/pip.2835.

[37] VDMA, International technology roadmap for photovoltaics (ITRPV), 2024.

[38] C. Peike, L. Purschke, K.-A. Weiss, M. Köhl, M. Kempe, Towards the origin of photochemical EVA discoloration, in: 2013 IEEE 39th Photovoltaic Specialists Conference, PVSC, 2013, pp. 1579–1584, http://dx.doi.org/10.1109/PVSC.2013.6744447.

[39] A. Sinha, H. Gopalakrishna, A. Bala Subramaniyan, D. Jain, J. Oh, D. Jordan, G. TamizhMani, Prediction of climate-specific degradation rate for photovoltaic encapsulant discoloration, IEEE J. Photovol. 10 (4) (2020) 1093–1101, http://dx.doi.org/10.1109/JPHOTOV.2020.2989182.

[40] Y. Lyu, J.H. Kim, X. Gu, Developing methodology for service life prediction of PV materials: Quantitative effects of light intensity and wavelength on discoloration of a glass/EVA/PPE laminate, Sol. Energy 174 (2018) 515–526, http://dx.doi.org/10.1016/j.solener.2018.08.067, URL https://www.sciencedirect.com/science/article/pii/S0038092X18308375.

[41] Iarc working group on the evaluation of carcinogenic risks to humans, in: Radiation, Lyon, 2012, Chapter 1. URL https://www.ncbi.nlm.nih.gov/books/NBK304366/.

[42] R. Meena, S. Kumar, R. Gupta, Comparative investigation and analysis of delaminated and discolored encapsulant degradation in crystalline silicon photovoltaic modules, Sol. Energy 203 (2020) 114–122, http://dx.doi.org/10.1016/j.solener.2020.04.041, URL https://www.sciencedirect.com/science/article/pii/S0038092X20304163.

[43] O.K. Segbefia, A.G. Imenes, T.O.S. tre, Moisture ingress in photovoltaic modules: A review, Sol. Energy 224 (2021) 889–906, http://dx.doi.org/10.1016/j.solener.2021.06.055, URL https://www.sciencedirect.com/science/article/pii/S0038092X21005375.

[44] A.A.Q. Hasan, A. Ahmed Alkahtani, S.A. Shahahmadi, M. Nur E. Alam, M.A. Islam, N. Amin, Delamination-and electromigration-related failures in solar panels—A review, Sustainability 13 (12) (2021) http://dx.doi.org/10.3390/su13126882, URL https://www.mdpi.com/2071-1050/13/12/6882.

[45] Y. Blom, D. Jimenez Pelarda, T. Minett, I. Kaaya, N. Kyranaki, R. Santbergen, O. Isabella, M. Ruben Vogt, Modelling moisture ingress in PV modules with different encapsulant and backsheet materials, Renew. Energy (2025) Submitted to.

[46] J. Zhu, M. Koehl, S. Hoffmann, K.A. Berger, S. Zamini, I. Bennett, E. Gerritsen, P. Malbranche, P. Pugliatti, A. Di Stefano, F. Aleo, D. Bertani, F. Paletta, F. Roca, G. Graditi, M. Pellegrino, O. Zubillaga, F.J.C. Iranzo, A. Pozza, T. Sample, R. Gottschalg, Changes of solar cell parameters during damp-heat exposure, Prog. Photovolt., Res. Appl. 24 (10) (2016) 1346–1358, http://dx.doi.org/10.1002/pip.2793, arXiv:https://onlinelibrary.wiley.com/doi/pdf/10.1002/pip.2793. URL https://onlinelibrary.wiley.com/doi/abs/10.1002/pip.2793.

[47] O.O. Ogbomo, E.H. Amalu, N. Ekere, P. Olagbegi, Effect of operating temperature on degradation of solder joints in crystalline silicon photovoltaic modules for improved reliability in hot climates, Sol. Energy 170 (2018) 682–693, http://dx.doi.org/10.1016/j.solener.2018.06.007, URL https://www.sciencedirect.com/science/article/pii/S0038092X18305462.

[48] H. Gopalakrishna, A. Sinha, J. Carpenter, S. Niverty, N. Chawla, D. Jordan, G. Tamizhmani, Activation energy for end-of-life solder bond degradation: Thermal cycling of field-aged PV modules, IEEE J. Photovol. 10 (6) (2020) 1762–1771, http://dx.doi.org/10.1109/JPHOTOV.2020.3025726.

[49] N. Bosco, T.J. Silverman, S. Kurtz, Climate specific thermomechanical fatigue of flat plate photovoltaic module solder joints, Microelectron. Reliab. 62 (2016) 124–129, http://dx.doi.org/10.1016/j.microrel.2016.03.024, URL https://www.sciencedirect.com/science/article/pii/S0026271416300609.

[50] J. Schmidt, A.G. Aberle, R. Hezel, Investigation of carrier lifetime instabilities in cz-grown silicon, in: Conference Record of the Twenty Sixth IEEE Photovoltaic Specialists Conference - 1997, 1997, pp. 13–18, http://dx.doi.org/10.1109/PVSC.1997.653914.

[51] J. Lindroos, H. Savin, Review of light-induced degradation in crystalline silicon solar cells, Sol. Energy Mater. Sol. Cells 147 (2016) 115–126, http://dx.doi.org/10.1016/j.solmat.2015.11.047, URL https://www.sciencedirect.com/science/article/pii/S0927024815006406.

[52] A. Herguth, Application of the concept of lifetime-equivalent defect density in defect systems comprising a multitude of defect species, Phys. Status Solidi (A) 216 (17) (2019) 1900322, http://dx.doi.org/10.1002/pssa.201900322, arXiv:https://onlinelibrary.wiley.com/doi/pdf/10.1002/pssa.201900322. URL https://onlinelibrary.wiley.com/doi/abs/10.1002/pssa.201900322.

[53] A. Herguth, On the meaning(fullness) of the intensity unit 'suns' in light induced degradation experiments, Energy Procedia 124 (2017) 53–59, http://dx.doi.org/10.1016/j.egypro.2017.09.339, 7th International Conference on Silicon Photovoltaics, SiliconPV 2017, 3-5 April 2017, Freiburg, Germany. URL https://www.sciencedirect.com/science/article/pii/S1876610217343102.

[54] H. Hashigami, Y. Itakura, T. Saitoh, Effect of illumination conditions on czochralski-grown silicon solar cell degradation, J. Appl. Phys. 93 (7) (2003) 4240–4245, http://dx.doi.org/10.1063/1.1559430, arXiv:https://pubs.aip.org/aip/jap/article-pdf/93/7/4240/19247263/4240_1_online.pdf.

[55] B. Sopori, P. Basnyat, S. Devayajanam, S. Shet, V. Mehta, J. Binns, J. Appel, Understanding light-induced degradation of c-si solar cells, in: 2012 38th IEEE Photovoltaic Specialists Conference, 2012, pp. 001115–001120, http://dx.doi.org/10.1109/PVSC.2012.6317798.

[56] D.A. Neamen, Semiconductor Physics and Devices, fourth ed., McGrawHill, 2011, p. 301.

[57] Desert Knowledge Australia Solar Centre, Trina, 5.3kw, mono-si, fixed, 2009, 2024, URL https://dkasolarcentre.com.au/source/alice-springs/dka-m6-b-phase. (Accessed 18 January 2024).

[58] S. Lindig, A. Curran, K. Rath, A. Khalilnejad, D. Moser, R.H. French, R. Wieser, IEA PVPS task 13-ST2.5: PLR determination benchmark study, 2024, http://dx.doi.org/10.17605/OSF.IO/VTR2S, URL https://osf.io/vtr2s/.

[59] NREL, PV data acquisition, 2024, URL https://developer.nrel.gov/docs/solar/pvdaq-v3/. (Accessed 18 January 2024).

[60] O.K. Segbefia, N. Akhtar, T.O. Sætre, Moisture induced degradation in field-aged multicrystalline silicon photovoltaic modules, Sol. Energy Mater. Sol. Cells 258 (2023) 112407, http://dx.doi.org/10.1016/j.solmat.2023.112407, URL https://www.sciencedirect.com/science/article/pii/S0927024823002283.

[61] E. Psimopoulos, J. Plautz, F. Fiedler, A. Augusto, Performance of a PV system operating for 30-years in scandinavia, in: 2024 IEEE 52nd Photovoltaic Specialist Conference, PVSC, 2024, pp. 0353–0355, http://dx.doi.org/10.1109/PVSC57443.2024.10748925.

[62] M. Roffeis, S. Kirner, J.-C. Goldschmidt, B. Stannowski, L.M. Perez, C. Case, M. Finkbeiner, New insights into the environmental performance of perovskite-on-silicon tandem solar cells – a life cycle assessment of industrially manufactured modules, Sustain. Energy Fuels 6 (2022) 2924–2940, http://dx.doi.org/10.1039/D2SE00096B.

[63] S. Mariotti, E. Köhnen, F. Scheler, K. Sveinbjörnsson, L. Zimmermann, M. Piot, F. Yang, B. Li, J. Warby, A. Musiienko, D. Menzel, F. Lang, S. Keßler, I. Levine, D. Mantione, A. Al-Ashouri, M.S. Härtel, K. Xu, A. Cruz, J. Kurpiers, P. Wagner, H. Köbler, J. Li, A. Magomedov, D. Mecerreyes, E. Unger, A. Abate, M. Stolterfoht, B. Stannowski, R. Schlatmann, L. Korte, S. Albrecht, Interface engineering for high-performance, triple-halide perovskite–silicon tandem solar cells, Science 381 (6653) (2023) 63–69, http://dx.doi.org/10.1126/science.adf5872.

[64] M. Kottek, J. Grieser, C. Beck, B. Rudolf, F. Rubel, World map of the Köppen-Geiger climate classification updated, Meteorol. Zeitschrif 15 (3) (2006) 259–263.

[65] J. Ascencio-Vásquez, K. Brecl, M. Topič, Methodology of Köppen-Geiger-photovoltaic climate classification and implications to worldwide mapping of PV system performance, Sol. Energy 191 (2019) 672–685, http://dx.doi.org/10.1016/j.solener.2019.08.072.

[66] F.J. Triana de las Heras, O. Isabella, M.R. Vogt, A machine learning approach to pv-climate classification, 2024, http://dx.doi.org/10.2139/ssrn.4905242.

[67] T. Dethe, H. Gill, D. Green, A. Greensweight, L. Gutierrez, M. He, T. Tajima, K. Yang, Causality and dispersion relations, Am. J. Phys. 87 (4) (2019) 279–290, http://dx.doi.org/10.1119/1.5092679.

[68] K. Ohta, H. Ishida, Comparison among several numerical integration methods for Kramers-Kronig transformation, Appl. Spectrosc. 42 (6) (1988) 952–957, URL https://opg.optica.org/as/abstract.cfm?URI=as-42-6-952.

[69] G. Belluardo, P. Ingenhoven, W. Sparber, J. Wagner, P. Weihs, D. Moser, Novel method for the improvement in the evaluation of outdoor performance loss rate in different PV technologies and comparison with two other methods, Sol. Energy 117 (2015) 139–152, http://dx.doi.org/10.1016/j.solener.2015.04.030, URL https://www.sciencedirect.com/science/article/pii/S0038092X15002182.

[70] L.C. Hirst, N.J. Ekins-Daukes, Fundamental losses in solar cells, Prog. Photovolt., Res. Appl. 19 (3) (2011) 286–293, http://dx.doi.org/10.1002/pip.1024, arXiv:https://onlinelibrary.wiley.com/doi/pdf/10.1002/pip.1024. URL https://onlinelibrary.wiley.com/doi/abs/10.1002/pip.1024.